Hall effect on the triangular lattice

G. León, C. Berthod, and T. Giamarchi
DPMC-MaNEP, University of Geneva, 24 Quai Ernest-Ansermet, 1211 Geneva 4, Switzerland

A. J. Millis
Physics Department, Columbia University, 538 West 120th Street, New York, New York 10027, USA
(Received 8 April 2008; published 6 August 2008)

We investigate the high-frequency Hall effect on a two-dimensional triangular lattice with nearest-neighbor hopping and a local Hubbard interaction. The complete temperature and doping dependencies of the high-frequency Hall coefficient R_H are evaluated analytically and numerically for small, intermediate, and strong interactions using various approximation schemes. We find that R_H follows the semiclassical $1/qn^*$ law near $T=0$ but exhibits a striking T-linear behavior with an interaction- and doping-dependent slope at high temperature. We compare our results with previous theories as well as Hall measurements performed in cobaltates.

DOI: 10.1103/PhysRevB.78.085105 PACS number(s): 71.27.+a, 71.18.+y, 72.15.Gd

I. INTRODUCTION

The interpretation of the Hall resistivity is made difficult even in relatively simple metals by the connection between the Hall constant and the relaxation time on the Fermi surface.[1] In many cases the simple semiclassical expression $R_H=1/qn^*$ does not work. We must therefore deal with a transport measurement encoding much more information than just the effective density n^* and the sign q of the charge carriers.

In strongly correlated systems, the Hall effect is even more difficult to interpret because interactions can have a large influence on the Hall resistivity. This influence moreover increases as the dimensionality of the systems decreases. There have been various attempts to describe the Hall effect in strongly correlated models with different geometries in two-dimensional (2D),[2,3] quasi-2D,[4] and quasi-one-dimensional (1D) (Refs. 5 and 6) systems. However a general theoretical understanding is still lacking.

Among the strongly correlated systems, the triangular lattice exhibits a unique property: It has the smallest possible closed loop with an odd number of steps (namely, three). Anderson[7] proposed that the model could have a spin-liquid ground state at commensurate fillings such as one electron per site. These peculiarities make the triangular lattice a very interesting system, which has been investigated extensively in the past decades. In particular, important differences between the Hall effect in the square and triangular lattices were pointed out in Ref. 2. Additionally, many studies have been motivated by the recent discovery of superconductivity in CoO_2 layered compounds (cobaltates),[8–11] which are good realizations of an isotropic 2D triangular lattice,[12] and in organic conductors of the bis(ethylenedithio) (BEDT) family,[13] where one finds various structures resembling the anisotropic triangular system.

Several Hall measurements have been undertaken in both organic superconductors[14,15] and cobaltates, especially in the Na_xCoO_2 compound.[16,17] In the latter, the anomalous linear increase in the dc Hall coefficient and a recent infrared Hall measurement[16] have motivated recent theoretical works[18–21] with the aim of investigating the role of correlations in the Hall effect. However many questions remain open. In the case of the organic conductors, the anisotropy present in the BEDT family complicates the problem further.

In the present work, we study theoretically the Hall effect in a 2D triangular lattice where electrons interact via an on-site Coulomb repulsion U. We calculate R_H in the high-frequency limit,[2,3] where the probing frequency ω is the largest energy scale of the problem. We cover the whole range of interaction values using several approximation schemes.

The paper is organized as follows: In Sec. II we introduce the model and the formalism used to compute the Hall coefficient R_H at high frequency. In Sec. III we present our analytical and numerical results obtained in the whole (n,U,T) parameter space. We discuss in detail the doping and temperature dependence of R_H. Section IV is devoted to a discussion of our results and a comparison with other theoretical approaches as well as experimental measurements. Finally our conclusions are given in Sec. V, and Appendixes A and C collect technical details.

II. MODEL AND METHOD

Our model is sketched in Fig. 1. We consider an anisotropic triangular lattice with nearest-neighbor hopping amplitudes t and t' and an on-site Hubbard interaction U. The Hamiltonian reads

$$\mathcal{H} = -\sum_{\langle ij\rangle\sigma} t_{ij} c^\dagger_{i\sigma} c_{j\sigma} + U\sum_i n_{i\uparrow} n_{i\downarrow}, \tag{1}$$

where $c^\dagger_\alpha$ (c_α) is the creation (annihilation) fermion operator, n_α is the fermionic number operator, and $\langle ij\rangle$ are nearest-neighboring sites. The dispersion relation for this model (Fourier transform of t_{ij}) is

$$\varepsilon_{\boldsymbol{k}} = -2t\cos(k_x a) - 4t'\cos(k_x a/2)\cos(k_y a\sqrt{3}/2). \tag{2}$$

The corresponding density of states (DOS) exhibits two Van Hove singularities which are degenerate when $t=t'$ (see Fig. 1). Unlike in the square lattice, the DOS has no particle-hole symmetry, irrespective of the values of t and t'.

We assume that a current I flows along the x axis and a dc magnetic field $\boldsymbol{B}$ is applied along z; hence a Hall voltage develops along the y axis (see Fig. 1). In order to represent the magnetic field and the applied ac electric field along x,

we use the vector potential $\boldsymbol{A}=\boldsymbol{A}^{\mathrm{mag}}+\boldsymbol{A}^{\mathrm{el}}$, where for the magnetic part we choose the Landau gauge, $\boldsymbol{A}^{\mathrm{mag}}=Bx\hat{\boldsymbol{y}}$, and $\boldsymbol{A}^{\mathrm{el}}$ describes the electric field. The coupling between the lattice fermions and the electromagnetic field induces a Peierls phase in the hopping amplitudes which change according to $t_{ij}\rightarrow t_{ij}\exp(-ie\int_i^j \boldsymbol{A}\cdot\boldsymbol{dl})$.

The operator for the total current, $J_\mu=\int d\boldsymbol{r} j_\mu(\boldsymbol{r})$, and the diamagnetic susceptibilities $\chi_\mu(0)$ of the system are defined as usual:

$$J_\mu = -S\sum_i \left.\frac{\delta\mathcal{H}}{\delta A_\mu(i)}\right|_{\boldsymbol{A}^{\mathrm{el}}=0}, \tag{3}$$

$$\chi_\mu(0) = -\frac{S}{N}\sum_i \left.\left\langle\frac{\delta^2\mathcal{H}}{\delta A_\mu^2(i)}\right\rangle\right|_{\boldsymbol{A}=0} = -\frac{2e^2}{NS}\sum_{\boldsymbol{k}}\frac{\partial^2\varepsilon_{\boldsymbol{k}}}{\partial k_\mu^2}\langle n_{\boldsymbol{k}}\rangle, \tag{4}$$

where $S=a^2\sqrt{3}/2$ is the unit-cell area, NS is the total system surface, $\langle n_{\boldsymbol{k}}\rangle=\langle c_{\boldsymbol{k}}^\dagger c_{\boldsymbol{k}}\rangle$ is the distribution function, and the thermodynamic average $\langle\cdots\rangle$ is taken with respect to the Hamiltonian in Eq. (1).

Performing the functional derivatives, we find for the components of the currents

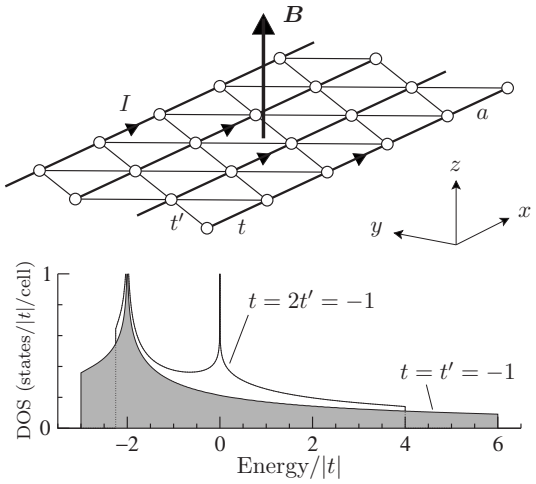

FIG. 1. Top: Two-dimensional triangular lattice. a is the lattice parameter; t and t' are the hopping amplitudes for bonds along the x direction and for $\pm 60°$ bonds, respectively. The current I flows along the x axis, the magnetic field $\boldsymbol{B}$ is applied along the z axis, and the Hall voltage is measured along the y axis. Bottom: Noninteracting density of states of the model in the cases $t=t'=-1$ and $t=2t'=-1$. The DOS generically presents two Van Hove singularities, which are degenerate in the isotropic lattice. The energy position of the Van Hove singularity for $t=t'=-1$ corresponds to a band filling of 1/2 electron per site (1/4 filling).

$$J_x = ea\left[2t\sum_{\boldsymbol{k}\sigma} c_{\boldsymbol{k}\sigma}^\dagger c_{\boldsymbol{k}\sigma}\sin(k_x a) + t'\sum_{\boldsymbol{k}\sigma}\sin\left(\frac{k_x a}{2}+\frac{\eta a}{4}\right)(c_{\boldsymbol{k}\sigma}^\dagger c_{\boldsymbol{k}+\boldsymbol{\eta}\sigma}e^{ik_y\sqrt{3}a/2}+\mathrm{H.c.})\right], \tag{5a}$$

$$J_y = -ea\sqrt{3}t'\sum_{\boldsymbol{k}\sigma}\cos\left(\frac{k_x a}{2}+\frac{\eta a}{4}\right)(ic_{\boldsymbol{k}\sigma}^\dagger c_{\boldsymbol{k}+\boldsymbol{\eta}\sigma}e^{ik_y\sqrt{3}a/2}+\mathrm{H.c.}), \tag{5b}$$

where we have defined the vector $\boldsymbol{\eta}=(\eta,0)$, with $\eta=\sqrt{3}eBa/2$. The diamagnetic susceptibilities resulting from Eqs. (4) and (2) are

$$\chi_x(0) = -\frac{4e^2}{\sqrt{3}}\frac{1}{N}\sum_{\boldsymbol{k}}\left[2t\cos(k_x a)+t'\cos\left(\frac{k_x a}{2}\right)\cos\left(k_y\sqrt{3}\frac{a}{2}\right)\right]\langle n_{\boldsymbol{k}}\rangle, \tag{6a}$$

$$\chi_y(0) = -\frac{4\sqrt{3}e^2t'}{N}\sum_{\boldsymbol{k}}\cos\left(\frac{k_x a}{2}\right)\cos\left(k_y\sqrt{3}\frac{a}{2}\right)\langle n_{\boldsymbol{k}}\rangle. \tag{6b}$$

The Hall coefficient is defined as the ratio of the Hall resistivity to the applied magnetic field, $R_H=\rho_{yx}/B$, the Hall resistivity ρ_{yx} being related to the conductivity tensor $\sigma_{\mu\nu}$ through

$$\rho_{yx} = \frac{\sigma_{xy}}{\sigma_{xx}\sigma_{yy}-\sigma_{xy}\sigma_{yx}}. \tag{7}$$

As shown in Appendix A, it is possible to rewrite R_H as a high-frequency series where the infinite-frequency limit reads

$$R_H(\omega\rightarrow\infty) = \lim_{B\rightarrow 0}\left(-\frac{i}{BNS}\frac{\langle[J_x,J_y]\rangle}{\chi_x(0)\chi_y(0)}\right) \tag{8}$$

and the remaining contributions are expressed in terms of a memory matrix.[3,22] Equation (8) was originally derived in Ref. 2 using a different frequency expansion. $R_H(\omega\rightarrow\infty)$ is expected to provide the dominant contribution at any finite frequency. The memory matrix formalism allows in principle going beyond the infinite-frequency approximation and compute corrections at finite frequency.[3,5] It leads, in particular,

to corrections due to interactions that vanish identically if $U=0$. These corrections do not affect the sign of R_H, which is entirely determined by $R_H(\omega\to\infty)$. In the following we shall consider only the infinite-frequency contribution to R_H, Eq. (8), and adopt the notation $R_H(\omega\to\infty)\equiv R_H$.

Strictly speaking, our results are valid provided the probing frequency is larger than any other energy scale in the system, $\omega>\max\{U,t,T\}$. The last two conditions, $\omega>\max\{t,T\}$, are easily fulfilled experimentally in known triangular compounds, while the condition $\omega>U$ is more problematic. However, as we will discuss in Sec. IV, in certain limits our results coincide with those obtained in Ref. 18 under the opposite assumption $\omega\ll U$, showing that this condition is not stringent.

In order to evaluate Eq. (8), we calculate the commutator $[J_x,J_y]$ from Eqs. (5a) and (5b), and we use the diamagnetic susceptibilities of Eq. (4) to arrive at

$$R_H=\frac{S}{e}\frac{\frac{1}{N}\sum_{\boldsymbol{k}}A_{\boldsymbol{k}}\langle n_{\boldsymbol{k}}\rangle}{\frac{1}{N}\sum_{\boldsymbol{k}}B_{\boldsymbol{k}}\langle n_{\boldsymbol{k}}\rangle\frac{1}{N}\sum_{\boldsymbol{k}}C_{\boldsymbol{k}}\langle n_{\boldsymbol{k}}\rangle},\tag{9}$$

with

$$A_{\boldsymbol{k}}=\cos\left(\frac{k_xa}{2}\right)\cos(k_xa)\cos\left(k_y\sqrt{3}\frac{a}{2}\right)+\frac{1}{4}\left(\frac{t'}{t}\right)[\cos(k_xa)+\cos(k_y\sqrt{3}a)],$$

$$B_{\boldsymbol{k}}=2\cos(k_xa)+\left(\frac{t'}{t}\right)\cos\left(\frac{k_xa}{2}\right)\cos\left(k_y\sqrt{3}\frac{a}{2}\right),$$

$$C_{\boldsymbol{k}}=\cos\left(\frac{k_xa}{2}\right)\cos\left(k_y\sqrt{3}\frac{a}{2}\right).\tag{10}$$

As can be seen from Eq. (9), the high-frequency Hall coefficient depends only on the distribution function $\langle n_{\boldsymbol{k}}\rangle$ as well as some geometrical factors. The interaction term in Eq. (1) therefore influences R_H only through its effect on $\langle n_{\boldsymbol{k}}\rangle$. Since $\langle n_{\boldsymbol{k}}\rangle$ depends relatively weakly on U, we also expect the U dependence of R_H to be weak. Another implication of Eq. (9) is that at low temperature the behavior of R_H can be interpreted in terms of an effective carrier concentration, as in the noninteracting case.

III. RESULTS

In the following we evaluate R_H in the whole domain of interaction values U with respect to the bandwidth $W=9t$ of the system by using four different approaches: exact calculation at $U=0$; a perturbative expansion of the self-energy at $U\lesssim W$; a local approximation to the self-energy, treated with dynamical mean-field theory (DMFT) at $U\gtrsim W$; and finally the atomic limit of the self-energy at $U\gg W$.

A. Noninteracting case

In the noninteracting case there are various limits in which we can obtain analytical results for R_H^0 (i.e., R_H at $U=0$): at zero temperature and band fillings near $n=0$ and $n=2$ and at high temperature $T\gg W$. For intermediate fillings and temperatures, we compute R_H^0 numerically by performing the sum in Eq. (9) on a dense 2048×2048 discrete $\boldsymbol{k}$-point mesh.

1. Zero temperature

Here we restrict for simplicity to the isotropic case $t'=t$ and we set the lattice parameter $a=1$. Close to the band edges, we can expand the various integrands of Eq. (10) and thus perform the $\boldsymbol{k}$ integrals.

Near the bottom of the band, the Fermi surface is made of two nearly circular electron pockets around $(\frac{4\pi}{3},0)$ and $(\frac{2\pi}{3},\frac{2\pi}{\sqrt{3}})$. In each pocket we have $\xi_{\boldsymbol{k}}\equiv\varepsilon_{\boldsymbol{k}}-\mu\approx3t-\frac{3}{4}tk^2-\mu$, where k is the momentum measured from the pocket center, and therefore $k_F^2=\frac{4}{3}(3-\mu/t)$. The corresponding electron density is $n=k_F^2/\pi$. Writing similar expansions of $A_{\boldsymbol{k}}$, $B_{\boldsymbol{k}}$, and $C_{\boldsymbol{k}}$ close to the pocket center and performing the Brillouin-zone integrations, we obtain the noninteracting Hall coefficient at low electron density:

$$R_H^0(T=0)=\frac{1}{ne}\left[1-\frac{3\pi n}{8}+\mathcal{O}(n^2)\right].\tag{11}$$

At sufficiently low density we recover, in the above expression, the classical result $R_H^0=1/ne$.

Near the top of the band, the Fermi surface is a nearly circular hole pocket centered at $\boldsymbol{k}=(0,0)$. Close to this point we have $\xi_{\boldsymbol{k}}\approx-6t+\frac{3}{2}tk^2-\mu$, and therefore $k_F^2=\frac{2}{3}(6+\mu/t)$. The corresponding density is obtained by subtracting the contribution of the hole pocket from the maximum density: $n_h=2-k_F^2/2\pi$. Similarly, for the functions $A_{\boldsymbol{k}}$, $B_{\boldsymbol{k}}$, and $C_{\boldsymbol{k}}$, we have to subtract the contribution of the hole pocket from the contribution of the whole Brillouin zone, which turns out to be zero because

$$\sum_{\boldsymbol{k}}A_{\boldsymbol{k}}=\sum_{\boldsymbol{k}}B_{\boldsymbol{k}}=\sum_{\boldsymbol{k}}C_{\boldsymbol{k}}=0.\tag{12}$$

Thus, for low hole densities $n_h=2-n$, we find that the noninteracting Hall coefficient is given by

$$R_H^0(T=0)=-\frac{1}{n_he}\left[1-\left(\frac{\pi n_h}{4}\right)^2+\mathcal{O}(n_h^3)\right],\tag{13}$$

and as $n_h\to0$ we have $R_H^0=-1/n_he$.

The complete density dependence of R_H^0 calculated numerically at zero temperature from Eq. (9) is displayed in Fig. 2 and compared to the limiting cases Eqs. (11) and (13). It is clear from this figure that the infinite-frequency R_H follows the well-known dependence of the dc Hall coefficient $R_H(\omega=0)$ on the carrier charge density. This indicates a weak frequency dependence of the noninteracting Hall coefficient

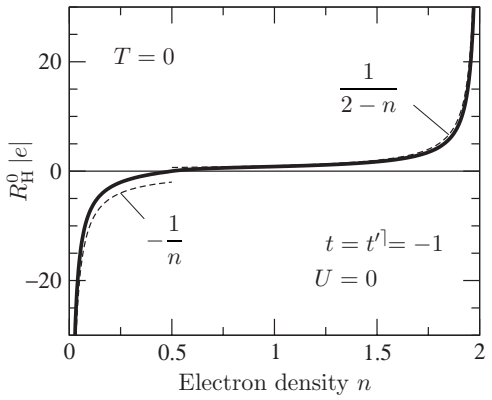

FIG. 2. Noninteracting Hall coefficient R_H^0 at zero temperature as a function of the electron density n for an isotropic triangular lattice with $t'=t=-1$. The dashed line indicates the classical behavior at low electron and hole carrier densities.

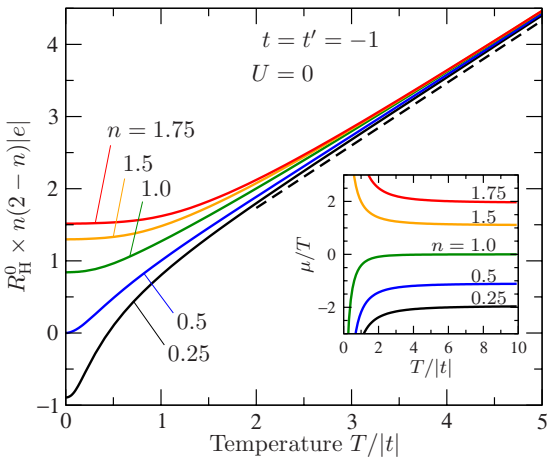

FIG. 3. (Color online) Temperature and electron density dependence of the noninteracting Hall coefficient R_H^0 for the isotropic triangular lattice with $t=t'=-1$. The dashed line shows the asymptotic behavior described by Eq. (16). Inset: Temperature and density dependence of the chemical potential μ, illustrating the relation $\mu\sim T$ at high temperature.

at zero temperature, since the dc result is recovered from the infinite-frequency limit of R_H. Furthermore this suggests, as we will discuss in detail below, that the frequency dependence should not be too crucial, even in the presence of interactions, for most band fillings. At $U=0$ the sign of the Hall coefficient is entirely given by the sign of the carriers. Moreover it can be seen from Fig. 2 how the sign changes at quarter filling when the Fermi energy crosses the Van Hove singularity of the DOS, and the Fermi-surface shape evolves from electronlike to holelike.

2. High temperature

If $T\gg t$ the distribution function $\langle n_k\rangle$, which reduces to the Fermi distribution at $U=0$, can be expanded in power of $\beta=1/T$. This expansion must be done at constant density n, which requires that $\beta\mu$ remains finite as $\beta\to 0$. In other words $\mu\sim T$ at high temperature. Taking this into account, we can deduce the relation between μ and n, $\exp(-\beta\mu)=2/n-1$, and write the Fermi distribution as

$$\langle n_k\rangle = \frac{n}{2} - n(2-n)\varepsilon_k\frac{\beta}{4} + \mathcal{O}(\beta^2). \tag{14}$$

Due to Eq. (12) the $\boldsymbol{k}$-independent terms in Eq. (14) do not contribute to R_H^0, which in this case takes the form

$$R_H^0(T\gg t) = -4T\frac{S}{e}\frac{1}{n(2-n)}\frac{\frac{1}{N}\sum_k A_k\varepsilon_k}{\frac{1}{N}\sum_k B_k\varepsilon_k\frac{1}{N}\sum_k C_k\varepsilon_k}. \tag{15}$$

Performing the Brillouin-zone integrations, we obtain

$$R_H^0(T\gg t) = \frac{T/t}{e}\frac{1}{n(2-n)}\frac{a^2\sqrt{3}}{2}\frac{3}{2+(t'/t)^2}. \tag{16}$$

This result is plotted in Fig. 3 together with the numerically calculated full temperature and density dependence. The most striking feature of Eq. (16) is the linear increase in R_H^0 with T. The same linear behavior was obtained in Ref. 23 at $\omega=0$, indicating a weak frequency dependence of R_H^0 at high temperature. Our result shows that the T-linear dependence of R_H is not due to interactions but to the peculiar topology of the triangular lattice. The sign of R_H^0 at high T is determined by the sign of t, irrespective of the density (see Fig. 3). We attribute this property to the fact that at high enough temperature, the full band contributes to the Hall effect. Hence the sign of R_H reflects the dominant nature, electronlike or holelike, of the band. As clear from Fig. 1, for $t<0$ the band is dominantly holelike, while for $t>0$ it is electronlike.

The relevance of result (16) is that even without interactions, the Hall coefficient has a linear dependence at high temperature due to the geometry of the system, emphasizing the peculiarity of the triangular lattice. By contrast, on the square lattice the same analysis yields a T-independent noninteracting $R_H^0=\frac{2}{e}[\frac{1}{n}-\frac{1}{n(2-n)}]$ at high temperature.

B. Weakly interacting regime

When interactions are present, the distribution function $\langle n_k\rangle$ can be expressed in terms of the one-electron self-energy $\Sigma(\boldsymbol{k},i\omega_n)$ as[24]

$$\langle n_k\rangle = \frac{1}{\beta}\sum_{\omega_n}\frac{e^{i\omega_n 0^+}}{i\omega_n-\xi_k-\Sigma(\boldsymbol{k},i\omega_n)}, \tag{17}$$

with $\omega_n=(2n+1)\pi T$ as the odd Matsubara frequencies. In the weak-coupling regime $U\lesssim W$, we evaluate the self-energy using conventional perturbation theory in U and we keep only the lowest-order contributions of order U^2. For a local interaction such as the Hubbard term in Eq. (1), there is only one diagram which is drawn in Fig. 4. The standard diagrammatic rules yield the following expression for the self-energy:

$$\Sigma(\boldsymbol{k}, i\omega_n) = -\frac{U^2}{N^2}\sum_{\boldsymbol{k}_1\boldsymbol{k}_2} \frac{f(\xi_{\boldsymbol{k}_2})[f(\xi_{\boldsymbol{k}_1}) - f(\xi_{\boldsymbol{k}+\boldsymbol{k}_1-\boldsymbol{k}_2})] - f(\xi_{\boldsymbol{k}_1})f(-\xi_{\boldsymbol{k}+\boldsymbol{k}_1-\boldsymbol{k}_2})}{i\omega_n + \xi_{\boldsymbol{k}_1} - \xi_{\boldsymbol{k}_2} - \xi_{\boldsymbol{k}+\boldsymbol{k}_1-\boldsymbol{k}_2}}, \tag{18}$$

where $f(\xi_{\boldsymbol{k}})$ is the Fermi distribution function.

The numerical evaluation of Eq. (18) is demanding due to the double momentum integration. This is particularly time consuming because our calculations are done at fixed density and thus require calculation of $\Sigma(\boldsymbol{k}, i\omega_n)$ many times in order to determine the chemical potential. However it turns out that the momentum dependence of $\Sigma(\boldsymbol{k}, i\omega_n)$ in Eq. (18) is weak. This is illustrated in Fig. 4, where we plot the Brillouin-zone average of the self-energy, $\bar{\Sigma}(i\omega_n)$, as well as its standard deviation. The weak momentum dependence allows us to compute $\Sigma(\boldsymbol{k}, i\omega_n)$ on a coarse (typically 16×16) $\boldsymbol{k}$-point mesh and then to interpolate using splines onto a dense mesh for the evaluation of $\langle n_{\boldsymbol{k}}\rangle$ and eventually R_H. The Matsubara sum in Eq. (17) also requires special attention: The formal regularization of the divergence through the exponential factor is not suitable for a numerical evaluation of the sum. We therefore rewrite Eq. (17) as

$$\langle n_{\boldsymbol{k}}\rangle = \frac{1}{2} + \frac{1}{\beta}\sum_{\omega_n}\left[\frac{1}{i\omega_n - \xi_{\boldsymbol{k}} - \Sigma(\boldsymbol{k}, i\omega_n)} - \frac{1}{i\omega_n}\right]. \tag{19}$$

The ω_n sum is now convergent and can be efficiently calculated via the truncation at some large frequency and the analytical evaluation of the remaining terms using an asymptotic expansion of the self-energy.

The R_H resulting from perturbation theory are valid in the regime $U < W \ll \omega$, with $W = 9|t|$ as the bandwidth of the system. As already anticipated the effect of a small U on the distribution $\langle n_{\boldsymbol{k}}\rangle$ is a subtle broadening. As a result the dependence of R_H on U is very weak at low U. Figure 5 provides an illustration of this weak dependence. As a consequence the noninteracting results in Sec. III A are expected to give a fairly good account of the Hall effect for an interaction strength smaller than the bandwidth W.

An important observation which we can make from our perturbative calculations is that the momentum dependence of the self-energy is very small; i.e., the self-energy is almost local in real space. This suggests approaching the strong-coupling regime $U \gtrsim W$ by assuming that the self-energy is *exactly* local. In Sec. III C we study such local approximations to the self-energy and we compare them to the result of the perturbation theory.

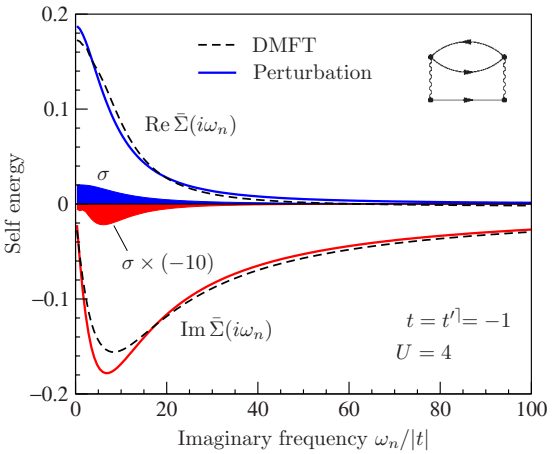

FIG. 4. (Color online) Brillouin-zone average of the real and imaginary parts of self-energy (18) at low temperature $T=0.1$, calculated using a 64×64 $\boldsymbol{k}$-point mesh (solid lines). The small standard deviations σ (shaded curves) illustrate the weak momentum dependence of $\Sigma(\boldsymbol{k}, i\omega_n)$. The dashed lines show the local self-energy resulting from the DMFT calculation (see Sec. III C 1). The density was set to $n=1.54$, which is the value for $Na_{0.7}CoO_2$ (see Sec. IV). Inset: Feynman diagram corresponding to Eq. (18).

C. Strongly interacting regime

Assuming that the self-energy is local in first approximation, we investigate here two models for $\Sigma(i\omega_n)$ and their implications for the Hall coefficient R_H. The first approach is based on DMFT (Ref. 25) and requires solving a difficult self-consistent quantum impurity problem. Due to numerical difficulties, this method cannot be pushed to very high interactions and/or very low temperature. Our second approach is based on a simple analytical form for $\Sigma(i\omega_n)$, which is expected to be valid at $U \gg W$, and allows us to express $\langle n_{\boldsymbol{k}}\rangle$ analytically in this limit.

1. DMFT

The DMFT approximation provides the exact solution of the problem under the assumption that the self-energy is local. In this framework the self-energy is expressed as

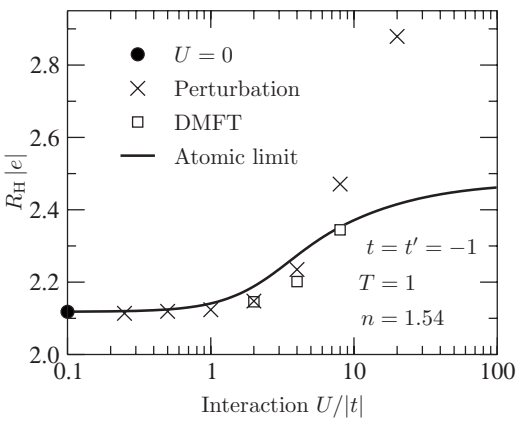

FIG. 5. Evolution of the high-frequency Hall coefficient with U calculated using different approximations at $T=|t|$ and $n=1.54$ for an isotropic triangular lattice with $t=t'=-1$.

$$\Sigma(i\omega_n) = \mathcal{G}_0^{-1}(i\omega_n) - \mathcal{G}^{-1}(i\omega_n), \tag{20}$$

where $\mathcal{G}_0$ is an effective propagator describing the time evolution of the fermions in the absence of interaction and $\mathcal{G}$ is the full propagator, which takes into account the local Hubbard interaction. The calculation of $\mathcal{G}$ from a given $\mathcal{G}_0$ amounts to solving the problem of a quantum impurity embedded in a bath. We do it by means of the quantum Monte Carlo Hirsch-Fye algorithm[26] as described in Ref. 25. From the requirement that $\mathcal{G}$ coincides with the local Green's function of the lattice, i.e.,

$$\mathcal{G}(i\omega_n) = \frac{1}{N}\sum_{\mathbf{k}} \frac{1}{i\omega_n - \xi_{\mathbf{k}} - \Sigma(i\omega_n)}, \tag{21}$$

one can deduce the self-consistency condition

$$\mathcal{G}_0^{-1}(i\omega_n) = 1/\tilde{D}[i\omega_n - \Sigma(i\omega_n)] + \Sigma(i\omega_n), \tag{22}$$

where $\tilde{D}(z) \equiv \int d\xi D(\xi)/(z-\xi)$ is the Hilbert transform of the DOS $D(\xi)$ corresponding to the triangular lattice and shown in Fig. 1. Once the self-consistent $\mathcal{G}_0(i\omega_n)$ is obtained, the corresponding self-energy $\Sigma(i\omega_n)$ is inserted into Eq. (19) to compute R_H.

In Fig. 4 we compare the DMFT self-energy with the Brillouin-zone average of perturbative expression (18), both calculated at $U=4$. It can be seen that the frequency dependence and the order of magnitude of the two quantities are very similar, suggesting that the self-energy is dominated by the U^2 term. Therefore the domain of validity of the perturbation theory is not limited to very small U. On the other hand it shows that the DMFT, although it is not a perturbative approach, provides a smooth transition from the weak- to the strong-coupling regime. This is further illustrated in Fig. 5, where we see that the values of R_H calculated by perturbation theory and DMFT coincide up to $U \approx 4|t|$. At not too low temperature, the DMFT calculation is reliable up to interaction strengths comparable to the bandwidth W. We have performed DMFT calculations at $U > W$; but since these results could be affected by systematic statistical errors in the Monte Carlo summation, they are not shown in Fig. 5. At $U \gg W$ it is expected that the DMFT result approaches the atomic limit, in which accurate calculations can be performed, as discussed in Sec. III C 2.

2. Atomic limit

In the limit of very strong interactions $U \gg W$ we assume that the self-energy approaches its atomic limit given by the expression (see Appendix C)

$$\Sigma_{\text{at}}(i\omega_n) = \frac{nU}{2} + \frac{n/2(1-n/2)U^2}{i\omega_n + \mu_{\text{at}} - (1-n/2)U}, \tag{23}$$

with μ_{at} as the chemical potential in the atomic limit, not to be confused with the lattice chemical potential μ. By using this expression in Eq. (17), it is possible to evaluate analytically the sum over Matsubara frequencies and thus to obtain a closed expression for $\langle n_{\mathbf{k}} \rangle$ (Appendix C). In Fig. 5 we show the Hall coefficient calculated with the atomic limit of the self-energy in the whole range of interaction values. R_H obviously converges to the noninteracting limit at low U since the atomic self-energy vanishes at $U=0$ and provides a good interpolation between the weak- and the strong-coupling regimes. At intermediate values $U \sim W$, the atomic limit is not reliable, although it gives the correct order of magnitude for R_H. Figure 5 also shows that R_H saturates at sufficiently large U.

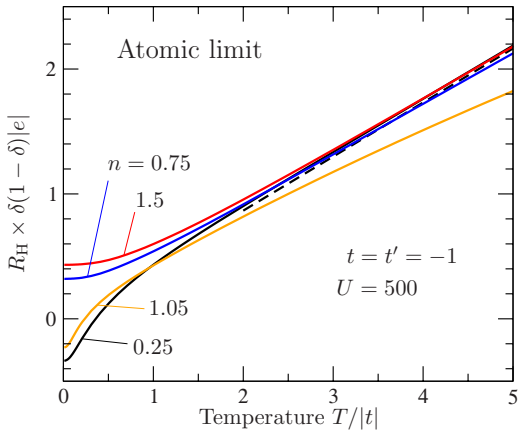

FIG. 6. (Color online) Temperature and density dependence of the high-frequency Hall coefficient calculated in the atomic limit at $U=500|t|$. The dashed line shows the asymptotic behavior, Eq. (24), and $\delta=|n-1|$. For densities close to half filling ($n=1.05$), $R_H(T)$ deviates from the asymptotic behavior (see text).

In Fig. 6 we display the temperature and density dependence of R_H at $U=500|t|$, which is a value typical for the cobaltate compounds as discussed in Sec. IV. We have selected four densities corresponding to the bottom and top of the lower and upper Hubbard bands (see also Fig. 8). Like for $U=0$ we find a T-linear increase in R_H at $T \gtrsim W$. Due to the Mott gap, however, the density dependence of the slope is not the same as for $U=0$. The slope can be obtained explicitly by sending U to $+\infty$ and performing the high-temperature expansion as in Sec. III A 2 (see Appendix C). The result is

$$R_H^{U=\infty}(T \gg t) = \frac{T/t}{e}\frac{1}{\delta(1-\delta)}\frac{a^2\sqrt{3}}{4}\frac{3}{2+(t'/t)^2}, \tag{24}$$

very similar to Eq. (16) except that the slope $\propto [4\delta(1-\delta)]^{-1}$ replaces $[2n(2-n)]^{-1}$, where $\delta=|n-1|$ measures the departure from half filling. The $U=\infty$ result of Eq. (24) is displayed in Fig. 6 and correctly describes our high-temperature results at $U=500|t|$. The differences observed at $n=1.05$ in Fig. 6 reflect the fact that close to half filling, the slope of the high-temperature R_H depends strongly on the interaction and is not saturated even at $U=500|t|$ (see also Fig. 7). Away from half filling, the U dependence of the slope is weaker, and Eq. (24) is valid for lower interaction values.

IV. DISCUSSION

The various approximations presented above allow us to calculate the Hall coefficient on the triangular lattice for all interactions strengths U and all temperatures T. The main limitation of our approach, in view of a comparison with

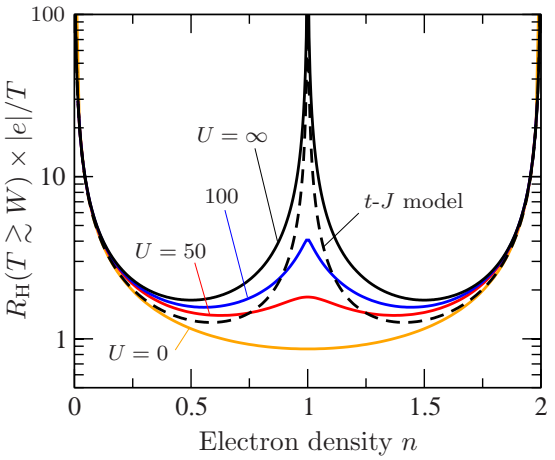

FIG. 7. (Color online) Density dependence of the Hall coefficient within the T-linear regime at $U=0$ and in the atomic limit at $U \gg |t|$ (solid lines), compared to the result of the t-J model (Ref. 18, dashed line).

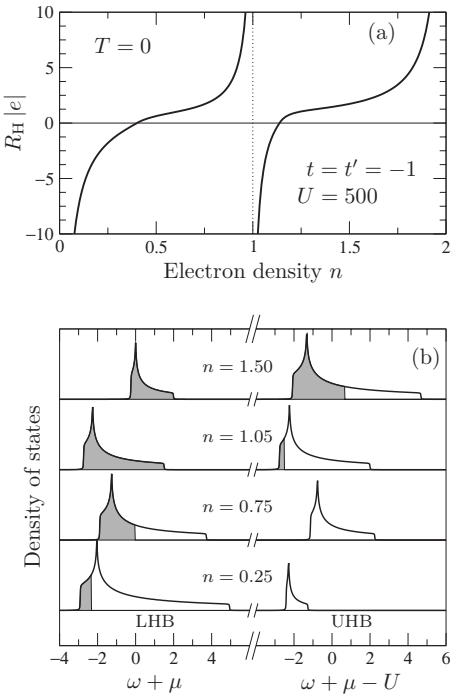

FIG. 8. (a) Density dependence of the Hall coefficient at $T=0$ and $U=500|t|$ calculated in the atomic-limit approximation. (b) Density of states for various electron densities, showing the lower (LHB) and upper (UHB) Hubbard bands. The shaded regions indicate the occupied states and the position of the chemical potential.

experimental systems, is that our results are in principle valid in the limit $W, U \ll \omega$ because they are based on a high-frequency expansion. The first criterion, $W \ll \omega$, is not too difficult to satisfy for realistic compounds if the measurement of the Hall effect is performed at optical frequencies. The second criterion, $U \ll \omega$, seems more problematic since interaction strengths can be as large as several electron volts, at the upper edge of the midultraviolet frequency domain. However, we have seen (Fig. 2) that at $U=0$ and $T=0$, the Hall coefficient calculated at $\omega=\infty$ coincides with the $\omega=0$ dc value. Moreover at $U=0$ and $T \gg t$, we obtained the $\omega=0$ results of Ref. 23. All this suggests that the frequency dependence of R_H is weak in the noninteracting case.

At the other extreme of the parameter space, $U=\infty$ and $T \gg W$, we can compare the result of the atomic-limit approximation with the result of the t-J model.[18] In the latter model U is considered infinite from the outset, so that the high-frequency and high-temperature expansion in Ref. 18 is in fact valid at frequencies $\omega < U$. We plot in Fig. 7 the density dependence of R_H obtained in both models at $U=\infty$ and $T \gtrsim W$. The small quantitative difference between the atomic limit at $U=\infty$ and the t-J model shows that these two ways of treating the $U=\infty$ limit are not equivalent: They differ, in particular, in the renormalization of the kinetic energy by the interaction. However the two models give, where they can be compared, very similar behaviors. This reinforces the idea that the frequency dependence of R_H is weak. Exact diagonalization on small clusters also indicate such a weak frequency dependence.[19] This strongly suggests that our results could also be valid at $\omega < U$ and could therefore be relevant in interpreting experiments performed in this regime. The atomic-limit approach has the advantage of giving access to the full temperature dependence (Fig. 6) as well as the U dependence, as shown in Fig. 7, while the calculation in Ref. 18 is valid at $U=\infty$ and $T \gg W$.

The evolution of R_H with temperature is of particular interest since it is most easily probed experimentally. A linear increase in R_H with temperature, without saturation at high T, was reported in Ref. 18 for the t-J model. Our results show that the Coulomb interaction is not responsible for this effect which is also present at $U=0$ (Fig. 3) and is therefore a consequence of the peculiar geometry of the triangular lattice. However the interaction controls the density dependence of the slope, which changes smoothly from $[2n(2-n)]^{-1}$ at $U=0$ to $[4\delta(1-\delta)]^{-1}$ at $U=\infty$. This is further corroborated in Fig. 7.

The sign of R_H turns out to be independent of n and U at high temperature, unlike in the square lattice, where R_H changes sign at $n=1$. The situation is different at $T=0$. In the noninteracting case R_H changes sign at quarter filling and can be simply interpreted in terms of the carrier density (Fig. 2). We have also investigated the $T=0$ density dependence of R_H at large U as shown in Fig. 8. The interpretation in terms of the carrier density remains qualitatively valid provided one takes into account the splitting of the DOS into the lower and upper Hubbard bands. These two bands are displayed in Fig. 8(b), where it can also be seen that the DOS keeps qualitatively the same shape as for $U=0$, but the width of each band varies strongly with the density n. Due to this band renormalization, the sign change of R_H at $n<1$ does not occur at quarter filling but a little below. Comparing Fig. 8(a) with Fig. 7, one easily understands why the temperature dependence of R_H is more pronounced slightly above $n=0$ and $n=1$, where R_H changes from negative at $T=0$ to positive at high T, than slightly below $n=1$ and $n=2$, where its stays positive (see also Fig. 6).

Among the Hall measurements reported for layered compounds with a triangular lattice structure, there is one performed at finite frequency by Choi *et al.*[16] on the cobaltate

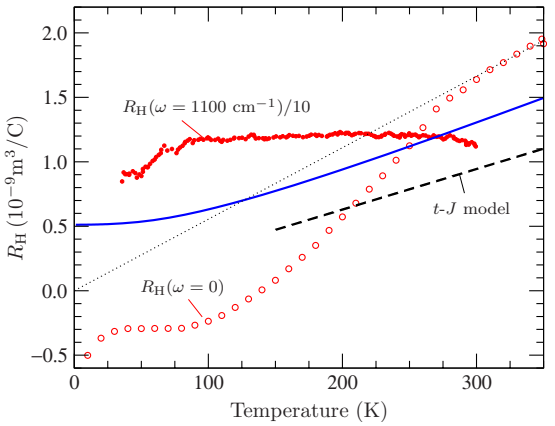

FIG. 9. (Color online) Comparison of the Hall coefficient in $Na_{0.7}CoO_2$ as measured by Choi *et al.* (Ref. 16) at $\omega=0$ (empty circles) and $\omega=1100\ \mathrm{cm}^{-1}$ (full circles) with available theoretical models. The blue solid line is the high-frequency result in the atomic limit and the dashed line shows the high-temperature result in the t-J model (Ref. 18). Theoretical curves are calculated at $t=t'=-10$ meV, $U=5$ eV, and $n=1.54$. The dotted line shows the best linear fit of the experimental data at high temperature (see text).

$Na_{0.7}CoO_2$. This material is composed of two-dimensional layers of edge-sharing CoO_6 octahedra separated by an insulating layer of Na^+ ions, leading to a triangular lattice of CoO_2 units.[27] Angle-resolved photoelectron spectroscopy (ARPES) measurements[8] indicate that the triangular lattice is isotropic with an estimated hopping amplitude of $t=-10$ meV and an effective Hubbard energy $U\sim 5$ eV. From the radius of the Fermi-surface hole pocket observed in ARPES, $k_F=0.65\pm 0.1\ \text{Å}^{-1}$, we deduce an electron density $n=1.54$. Choi *et al.*[16] measured the temperature dependence of both the dc and ac Hall coefficients up to room temperature. The ac measurement was performed at $\omega=1100\ \mathrm{cm}^{-1}\approx 12|t|$. The experimental conditions thus satisfy $T,W<\omega\ll U$.

The behavior of the dc R_H above $T=250$ K is consistent with the linear increase predicted by the various theoretical models. By adjusting these models on the dc experimental data at high temperature (dotted line in Fig. 9), we obtain independent determinations of the hopping amplitude t, namely, $t=-7.4$ meV using atomic-limit model (24) and $t=-5.7$ meV using the t-J model. These values are in good agreement with the ARPES results. We note, however, that there are discrepancies between different sets of experimental data.[16,17]

The organic conductors of the BEDT family present several compounds with an anisotropic triangular structure. Unfortunately we are not aware of any measurements of the ac Hall effect which we could compare to our calculations, although measurements have been done at zero frequency in these materials.[14,15]

V. CONCLUSION

The theoretical high-frequency Hall coefficient in the two-dimensional triangular lattice exhibits two different characteristic behaviors at low and high temperatures: Near $T=0$, R_H resembles the classical dc Hall coefficient $1/qn^*$, where q and n^* are the carrier charge and density, respectively. At temperatures higher than the bandwidth, R_H shows a remarkable T-linear behavior with a density- and interaction-dependent slope. These conclusions apply provided the probing frequency is larger than the other energy scales of the problem and that the electron self-energy remains essentially local for strong interactions.

Although we argued that the frequency dependence of R_H is probably weak, it is clear that for understanding the anomalously large $R_H(\omega)$ measured experimentally in $Na_{0.7}CoO_2$ in the midinfrared range, one would have to extend the approach in order to cover the domain of intermediate frequencies. Concerning the self-energy, we do not exclude that this quantity could present a non-negligible momentum dependence for strong interactions. This could affect the Hall coefficient, especially at low temperature. Such a momentum dependence is indeed expected for ordered ground states at and close to half filling due to antiferromagnetism. However, the influence of a momentum-dependent self-energy would be reduced on the Hall effect because expression (9) for the Hall coefficient averages the distribution function over the Brillouin zone. In addition we do not expect a strong momentum dependence far from half filling, as in the case of the $n=1.54$ cobaltate considered here.

Another possibility is that the simple one-band model considered in this study would not suffice to capture the detailed properties of the materials.[28] Experiments conducted as a function of ω, as well as measurements of other materials with a triangular structure, would be very helpful in elucidating the peculiarities of the Hall effect in triangular compounds.

ACKNOWLEDGMENTS

The authors are grateful to B. S. Shastry and H. D. Drew for valuable discussions. This work was supported by the Swiss National Science Foundation through Division II and MaNEP and by Grant No. NSF-DMR-0707847.

APPENDIX A: MEMORY MATRIX FORMALISM

The use of the memory matrix allows one to perform finite-order frequency expansions, which are singular for the conductivities due to their resonance structure.[22] This approach has been used in previous works to study transport properties in Luttinger liquids,[29] as well as the Hall effect in the 2D Hubbard model[3] and in quasi-one-dimensional systems.[5]

As we want to calculate the Hall resistivity ρ_{yx}, we start from the general relation between ρ_{yx} and the conductivity tensor $\sigma_{\mu\nu}$:

$$\rho_{yx}=\frac{\sigma_{xy}}{\sigma_{xx}\sigma_{yy}+\sigma_{xy}^2}. \tag{A1}$$

Then we rewrite the conductivity tensor in terms of a memory matrix $\boldsymbol{M}(\omega)$ as[22]

$$i\boldsymbol{\sigma}(\omega) = \boldsymbol{\chi}(0)[\omega\mathbb{1} + \boldsymbol{\Omega} + i\boldsymbol{M}(\omega)]^{-1}, \tag{A2}$$

where $\boldsymbol{\sigma}^T$ denotes the transpose of $\boldsymbol{\sigma}$, $\boldsymbol{\Omega}$ is called the frequency matrix, and $\boldsymbol{M}(\omega)$ is the memory matrix. $\boldsymbol{\chi}(0)$ is a diagonal matrix composed of the diamagnetic susceptibilities in each direction, $\chi_{\mu\nu}(0) = \delta_{\mu\nu}\chi_\mu(0)$. The frequency matrix $\boldsymbol{\Omega}$ in Eq. (A2) is defined in terms of the equal-time current-current correlators as[3]

$$\Omega_{\mu\nu} = \frac{1}{\mathcal{S}\chi_\mu(0)}\langle[J_\mu, J_\nu]\rangle, \tag{A3}$$

with $\mathcal{S}$ as the sample surface (in a two-dimensional system). Now we invert Eq. (A2) and express the memory matrix $\boldsymbol{M}$ in terms of the conductivity tensor. For the Hall coefficient R_H, we need only the off-diagonal term M_{xy} given by

$$iM_{xy}(\omega) = \frac{i\chi_y(0)\sigma_{xy}(\omega)}{\sigma_{xx}(\omega)\sigma_{yy}(\omega) + \sigma_{xy}^2(\omega)} - \Omega_{xy}. \tag{A4}$$

This implies that the Hall coefficient $R_H = \rho_{yx}/B$ can be expressed in term of the frequency and memory matrices as

$$R_H(\omega) = \frac{1}{i\chi_y(0)}\lim_{B\to 0}\frac{\Omega_{xy} + iM_{xy}(\omega)}{B}. \tag{A5}$$

Since the memory matrix vanishes as ω^{-2} at high frequency, we see that the Hall coefficient is given by Eq. (8) in the infinite-frequency limit.

APPENDIX B: CALCULATION OF THE DMFT SELF-ENERGY

We evaluate the local self-energy in the DMFT framework using the Hirsch-Fye algorithm[26] as described in Ref. 25. In this method the imaginary-time axis $[0, \beta[$ is cut into L slices, and the Trotter formula is used in each time slice in order to single out the Hubbard interaction. In a second step the interaction is decoupled via the introduction of an Ising variable in every time slice. Green's function $\mathcal{G}(\tau)$ is finally calculated by averaging over the ensemble of configurations of the Ising variables using a Monte Carlo sampling and local updates. In our calculations at $\beta = 1$ and $U \leq 20$, we take $L = 128$ and we keep 10^6 out of the $\sim 10^8$ configurations visited. The numerical accuracy of the calculated $\mathcal{G}(\tau)$ is estimated to be $\sim 10^{-3}$ at the highest U values and closer to 10^{-4} at $U \lesssim 8$. We believe that the accuracy at $U > 8$ is not sufficient to get a reliable self-energy; hence we did not evaluate R_H at $U > 8$ in Fig. 5.

In order to calculate the self-energy and solve the DMFT self-consistency condition, Eq. (22), we need to Fourier transform $\mathcal{G}(\tau)$ from imaginary time to imaginary Matsubara frequencies $i\omega_n$. In traditional implementations of the algorithm, this step is performed through a cubic spline interpolation of $\mathcal{G}(\tau)$. Because cubic splines are nonanalytic, however, the resulting Fourier series are unreliable at frequencies above $\sim L/\beta$. Instead of an interpolation, we have performed a fit of $\mathcal{G}(\tau)$. Our fitting function is a discrete form of the spectral representation, $\mathcal{G}(\tau) = -\int d\varepsilon A(\varepsilon) e^{-\varepsilon\tau} f(-\varepsilon)$, which we express as

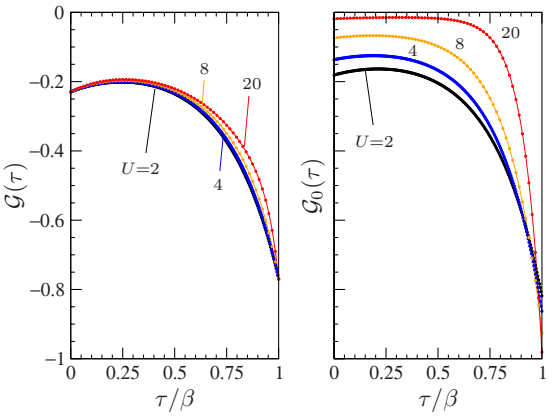

FIG. 10. (Color online) DMFT imaginary-time propagators calculated at $\beta = 1$ and $n = 1.54$ for various interaction strengths. The symbols show the QMC results on the discrete-time mesh. The solid lines are the fit, Eq. (B1), used to evaluate the self-energy shown in Fig. 4.

$$\mathcal{G}(\tau) = -\sum_{j=1}^{M} A_j e^{-\varepsilon_j\tau} f(-\varepsilon_j), \tag{B1}$$

with $A_j \geq 0$ and $\Sigma_{j=1}^{M} A_j = 1$. The number M of poles ε_j and their weight A_j are determined by adding more and more terms in Eq. (B1) until the fitted function matches all quantum Monte Carlo (QMC) data points within a numerical tolerance, which we take as the estimated accuracy of $\mathcal{G}(\tau)$. The Fourier transform is then simply

$$\mathcal{G}(i\omega_n) = \sum_{j=1}^{M} \frac{A_j}{i\omega_n - \varepsilon_j}. \tag{B2}$$

The calculated self-consistent propagators $\mathcal{G}(\tau)$ and $\mathcal{G}_0(\tau)$ are displayed in Fig. 10, together with the fits to Eq. (B1).

Solving Eq. (22) at fixed electron density requires determination of the chemical potential μ self-consistently. In our calculations we perform the search for both the self-consistent $\mathcal{G}_0$ and μ in one shot using a global minimization procedure. As a result the self-consistent solution can be reached in typically less than 20 iterations.

APPENDIX C: SELF-ENERGY AND DISTRIBUTION FUNCTION IN THE ATOMIC LIMIT

In the case $U \gg t$ one can treat Hamiltonian (1) using a perturbative expansion in t_{ij}/U. The atomic limit is the zeroth-order term of this development, and it corresponds to a collection of disconnected sites with four possible states on each site. This limit is not very useful since there is no hopping and thus no possible transition below the Hubbard energy U. In order to retain the low-energy dynamics of the problem, we adopt a hybrid approach, where the free dispersion is used in the lattice Green's function together with the self-energy evaluated in the atomic limit. The atomic self-energy is obtained by diagonalizing Hamiltonian (1) with $t_{ij} = 0$, which leads to the atomic Green's function

$$G_{\rm at}(i\omega_n) = \frac{1-n/2}{i\omega_n+\mu_{\rm at}} + \frac{n/2}{i\omega_n+\mu_{\rm at}-U}, \tag{C1}$$

while the noninteracting $G_{0,\rm at}=1/(i\omega_n+\mu_{\rm at})$ results by putting $U=0$. From Dyson's equation, $\Sigma=G_0^{-1}-G^{-1}$, we deduce the atomic self-energy displayed in Eq. (23). Here $\mu_{\rm at}$ is the chemical potential in the *true* atomic limit—i.e., the limit where the lattice Green's function takes form (C1). Therefore the electron density is given by $n=(2-n)f(-\mu_{\rm at})+nf(U-\mu_{\rm at})$, with f as the Fermi function. We can invert this relation and express $\mu_{\rm at}$ explicitly in terms of the electron density as

$$\mu_{\rm at} = -\frac{1}{\beta}\log\left[\frac{1}{n}-1+\sqrt{\left(\frac{1}{n}-1\right)^2+e^{-\beta U}\left(\frac{2}{n}-1\right)}\right].$$

Using atomic self-energy (23) as an approximation to the exact self-energy in Eq. (17), we evaluate analytically the lattice distribution function $\langle n_{\boldsymbol{k}}\rangle$. Let us first remark that

$$\frac{1}{i\omega_n-\xi_{\boldsymbol{k}}-\Sigma_{\rm at}(i\omega_n)} = \frac{Z_{\boldsymbol{k}}}{i\omega_n-E_{\boldsymbol{k}}^+} + \frac{1-Z_{\boldsymbol{k}}}{i\omega_n-E_{\boldsymbol{k}}^-},$$

with

$$E_{\boldsymbol{k}}^{\pm} = (\xi_{\boldsymbol{k}} \pm \Delta_{\boldsymbol{k}} + U - \mu_{\rm at})/2,$$

$$Z_{\boldsymbol{k}} = \frac{\xi_{\boldsymbol{k}}+\Delta_{\boldsymbol{k}}+U-\mu_{\rm at}}{4\Delta_{\boldsymbol{k}}} \times \frac{(\xi_{\boldsymbol{k}}+\Delta_{\boldsymbol{k}}-U+\mu_{\rm at})(\mu_{\rm at}-U+nU/2)+n\mu_{\rm at}U}{\xi_{\boldsymbol{k}}(\mu_{\rm at}-U+nU/2)+n\mu_{\rm at}U/2},$$

$$\Delta_{\boldsymbol{k}} = \sqrt{(\xi_{\boldsymbol{k}}+U+\mu_{\rm at})^2+2(n-2)(\xi_{\boldsymbol{k}}+\mu_{\rm at})U}.$$

As a result the Matsubara sum in Eq. (17) is easily performed to yield

$$\langle n_{\boldsymbol{k}}\rangle_{\rm at} = Z_{\boldsymbol{k}} f(E_{\boldsymbol{k}}^+) + (1-Z_{\boldsymbol{k}}) f(E_{\boldsymbol{k}}^-). \tag{C2}$$

Within this approximation it is also straightforward to perform the infinite U limit. Taking into account that both μ and $\mu_{\rm at}$ are either of order t (if $n<1$) or of order U (if $n>1$), we find that $Z_{\boldsymbol{k}}$ approaches $n/2$ as U increases toward $+\infty$. Likewise, if $n<1$ we have $E_{\boldsymbol{k}}^+\sim U$ and $E_{\boldsymbol{k}}^-\sim t$, while if $n>1$ we have $E_{\boldsymbol{k}}^+\sim t$ and $E_{\boldsymbol{k}}^-\sim -U$. Hence we find

$$\langle n_{\boldsymbol{k}}\rangle_{\rm at}^{U=\infty} = \begin{cases} \left(1-\frac{n}{2}\right) f\left[\left(1-\frac{n}{2}\right)\xi_{\boldsymbol{k}} - \frac{n}{2}\mu_{\rm at}\right], & n<1 \\ \frac{n}{2} f\left[\frac{n}{2}\tilde{\xi}_{\boldsymbol{k}} - \left(1-\frac{n}{2}\right)\tilde{\mu}_{\rm at}\right] + 1 - \frac{n}{2}, & n>1, \end{cases}$$

where we have introduced $\tilde{\mu}_{\rm at}\equiv\mu_{\rm at}-U=-\frac{1}{\beta}\log[(1-n/2)/(n-1)]$ and $\tilde{\xi}_{\boldsymbol{k}}\equiv\varepsilon_{\boldsymbol{k}}-\tilde{\mu}$, with $\tilde{\mu}=\mu-U$. For the purpose of evaluating the high-temperature behavior of the Hall coefficient at $U=\infty$, we finally expand the distribution function in powers of β following the procedure described in Sec. III A 2:

$$\langle n_{\boldsymbol{k}}\rangle_{\rm at}^{U=\infty} = \begin{cases} \frac{n}{2} - n(1-n)\varepsilon_{\boldsymbol{k}}\frac{\beta}{2} + \mathcal{O}(\beta^2), & n<1 \\ \frac{n}{2} - (n-2)(1-n)\varepsilon_{\boldsymbol{k}}\frac{\beta}{2} + \mathcal{O}(\beta^2), & n>1. \end{cases}$$

Comparing with Eq. (14), which is valid at $U=0$, we see that the only difference between the high-temperature behaviors of R_H at $U=0$ and $U=\infty$ is the n-dependent slope, and we easily deduce that

$$R_H^{U=\infty}(T\gg t) = \begin{cases} \frac{T/t}{e}\frac{1}{n(1-n)}\frac{a^2\sqrt{3}}{4}\frac{3}{2+(t'/t)^2}, & n<1 \\ \frac{T/t}{e}\frac{1}{(n-2)(1-n)}\frac{a^2\sqrt{3}}{4}\frac{3}{2+(t'/t)^2}, & n>1. \end{cases}$$

By introducing $\delta=|n-1|$, which measures the doping with respect to half filling, these two cases can be recast in one single expression shown in Eq. (24).

[1] N. Ashcroft and N. Mermin, *Solid State Physics* (Saunders, Philadelphia, 1976).
[2] B. S. Shastry, B. I. Shraiman, and R. R. P. Singh, Phys. Rev. Lett. **70**, 2004 (1993).
[3] E. Lange, Phys. Rev. B **55**, 3907 (1997).
[4] V. M. Yakovenko and A. T. Zheleznyak, Synth. Met. **120**, 1083 (2001).
[5] G. León, C. Berthod, and T. Giamarchi, Phys. Rev. B **75**, 195123 (2007).
[6] G. León and T. Giamarchi, J. Low Temp. Phys. **142**, 315 (2006).
[7] P. W. Anderson, Science **235**, 1196 (1987).
[8] M. Hasan *et al.*, Phys. Rev. Lett. **92**, 246402 (2004).
[9] K. Takada, H. Sakurai, E. Takayama-Muromachi, F. Izumi, R. A. Dilanian, and T. Sasaki, Nature (London) **422**, 53 (2003).
[10] D. Qian, L. Wray, D. Hsieh, L. Viciu, R. J. Cava, J. L. Luo, D. Wu, N. L. Wang, and M. Z. Hasan, Phys. Rev. Lett. **97**, 186405 (2006).
[11] J. Laverock *et al.*, Phys. Rev. B **76**, 052509 (2007).
[12] D. J. Singh, Phys. Rev. B **61**, 13397 (2000).
[13] H. Seo, C. Hotta, and H. Fukuyama, Chem. Rev. (Washington, D.C.) **104**, 5005 (2004).
[14] Y. V. Sushko, N. Shirakawa, K. Murata, Y. Kubo, N. D. Kushch, and E. B. Yagubskii, Synth. Met. **85**, 1541 (1997).
[15] K. Katayama, T. Nagai, H. Taniguchi, K. Satoh, N. Tajima, and R. Kato, J. Low Temp. Phys. **142**, 519 (2007).
[16] E. J. Choi, S. H. Jung, J. H. Noh, A. Zimmers, D. Schmadel, H. D. Drew, Y. K. Bang, J. Y. Son, and J. H. Cho, Phys. Rev. B **76**, 033105 (2007).
[17] Y. Wang, N. S. Rogado, R. J. Cava, and N. P. Ong, Nature (London) **423**, 425 (2003).
[18] B. Kumar and B. S. Shastry, Phys. Rev. B **68**, 104508 (2003).
[19] J. O. Haerter, M. R. Peterson, and B. S. Shastry, Phys. Rev. B **74**, 245118 (2006).
[20] W. Koshibae, A. Oguri, and S. Maekawa, Phys. Rev. B **75**,

205115 (2007).
[21] J. O. Haerter, M. R. Peterson, and B. S. Shastry, Phys. Rev. Lett. **97**, 226402 (2006).
[22] W. Götze and P. Wölfle, Phys. Rev. B **6**, 1226 (1972).
[23] O. I. Motrunich and P. A. Lee, Phys. Rev. B **69**, 214516 (2004).
[24] G. D. Mahan, *Many Particle Physics* (Plenum, New York, 1981).
[25] A. Georges, G. Kotliar, W. Krauth, and M. J. Rozenberg, Rev. Mod. Phys. **68**, 13 (1996).
[26] J. E. Hirsch and R. M. Fye, Phys. Rev. Lett. **56**, 2521 (1986).
[27] J. Y. Son, B. G. Kim, and J. H. Chon, Appl. Phys. Lett. **86**, 221918 (2005).
[28] C. Weber, A. Läeuchli, F. Mila, and T. Giamarchi, Phys. Rev. B **73**, 014519 (2006).
[29] T. Giamarchi, Phys. Rev. B **44**, 2905 (1991).